



Electrosprayed graphene decorated with ZnO nanoparticles for supercapacitors

Edmund Samuel^{a,1}, Priyanka U. Londhe^{a,1,b}, Bhavana Joshi^{a,1}, Min-Woo Kim^a, Karam Kim^a, Mark T. Swihart^c, Nandu B. Chaure^b, Sam S. Yoon^{a,*}

^a School of Mechanical Engineering, Korea University, Seoul 02841, Republic of Korea

^b Department of Physics, Savitribai Phule Pune University (formerly University of Pune), Pune 411007, India

^c Department of Chemical & Biological Engineering, University at Buffalo, The State University of New York, Buffalo, NY 14260-4200, USA

ARTICLE INFO

Article history:

Received 19 September 2017

Received in revised form

12 December 2017

Accepted 26 December 2017

Available online 12 January 2018

ABSTRACT

A binder-free nanocomposite consisting of ZnO nanoparticles (NPs) grown directly on graphene sheets by electrospraying was fabricated for use as an electrode material in supercapacitors. The optimal concentrations of graphene and ZnO NPs were determined from the capacitive characteristics of the composite. Scanning electron microscopy confirmed that the ZnO NPs grew in a uniformly distributed manner on the graphene sheets and that they exhibited negligible agglomeration. Further, X-ray diffraction analysis confirmed that ZnO growth was preferentially oriented along (100) plane in the ZnO/graphene composite. A symmetric supercapacitor fabricated using this composite exhibited an energy density of $67 \text{ mWh} \cdot \text{cm}^{-3}$ and power density of $6000 \text{ mW} \cdot \text{cm}^{-3}$. The composite also showed good long-term cycling performance, retaining 90% of its capacitance after 1000 galvanostatic charge/discharge cycles.

© 2018 Elsevier B.V. All rights reserved.

1. Introduction

Increase in the demand for renewable energy resources as well as devices for storing the generated energy have propelled the development of energy conversion and storage devices such as batteries, fuel cells, and supercapacitors (SCs) [1–3]. SCs, also known as electrochemical supercapacitors, are being explored as alternatives to batteries owing to their high charge/discharge rate, high power density, and long cycling lifetime and are expected to find use in a wide range of applications [4–6]. Based on their charge storage mechanism, SCs can be categorized as electrical double-layer capacitors (EDLCs) and pseudocapacitors. EDLCs, such as those fabricated using carbon-based materials, store charge through electrostatic adsorption at the electrode/electrolyte interface. On the other hand, pseudocapacitors store charge through fast reversible faradaic (redox) reactions that occur in the electrode material and involve the transport of charge across a double layer, in a manner similar to that seen in batteries [7–9]. Transition metal

oxides/hydroxides and conducting polymers are known to show pseudocapacitance.

Inorganic oxide materials such as SnO_2 [10], MnO_2 [11,12], RuO_2 [13], NiO [14], and ZnO [15–17] have received significant attention as materials for forming SC electrodes as they undergo fast and reversible redox reactions [18]. Nanostructures of these materials show improved performance due to their higher surface-to-volume ratio and a shorter ion diffusion path length. In addition, they allow for the control of electron and ion transport, resulting in a greater number of electrochemically active sites for charge transfer. ZnO nanoparticles (NPs) are particularly attractive for use as an electrode material in SCs because of their high electrochemical activity, nontoxicity, ease of synthesis, low cost, and desirable morphological features [19,20]. However, a major challenge with using ZnO is its capacity decay with long-term cycling owing to its poor electronic conductivity as well as the agglomeration of ZnO NPs.

A straightforward strategy for overcoming the above-mentioned inadequacies of ZnO NPs is to fabricate composites of the NPs with carbon-based materials such as carbon nanotubes (CNTs; 1D) and graphene, to improve the conductivity of ZnO and reduce the agglomeration of the ZnO NPs. Furthermore, graphene, which consists of 2D carbon monolayers, is highly suited for use in SCs. Few-layered graphene contains a large number of ion

* Corresponding author.

E-mail address: skyoons@korea.ac.kr (S.S. Yoon).

¹ Equal contribution.

adsorption sites owing to its high surface area [21,22]. However, graphene does not exhibit a high capacitance when used alone in SCs, as the van der Waals interactions result in the restacking of the graphene sheets, and hence a decrease in the capacitance [23,24]. Creating a composite of graphene and NPs of a material such as ZnO can prevent the restacking of the graphene sheets while simultaneously increasing the conductivity of the ZnO NPs. Attractive interactions between the graphene sheets and ZnO NPs can be controlled to produce a uniform dispersion of the NPs over the graphene surface, resulting in a composite that has a controlled morphology and exhibits reduced particle agglomeration. Through these synergistic effects, ZnO/graphene composites are expected to show improved electrochemical properties in SCs.

Several methods have been proposed for synthesizing ZnO/graphene composites, such as the solvothermal method [25], spray pyrolysis [26] and microwave-assisted synthesis [27], among others. However, these methods are multistep processes in which particles of the synthesized composite must be purified by centrifugation (or another method) to remove the byproducts formed during the synthesis reaction. The electrodes are then prepared by coating a paste of a conducting agent, a binder, and the active material on the collector substrate. The binders used for preparing the electrode remains as a residual impurity and may adversely affect the electrochemical properties of the active material. Arvinda et al. [20] fabricated a ZnO/CNT-based binder-free SC electrode by vacuum-based DC magnetron sputtering, which is a relatively expensive technique. Further, most methods for forming ZnO nanostructures are complex or require the use of high vacuum. Thus, a facile and low-cost process for preparing ZnO/carbon composites that show improved electrode performance could be of significant value.

The sol-gel method [28], electrodeposition [29], chemical bath deposition [30], and electro spraying [31] are all low-cost non-vacuum-based techniques. Of these, electro spray deposition (ESD) is one of the most economical ones and is used widely for producing a range of devices such as solar cells, water splitting devices, and gas sensors, to name a few [31,32]. During ESD, a high potential is maintained at the nozzle dispensing the liquid over the grounded substrate, resulting in the elongation of the meniscus and the formation of a cone jet. Very fine monodisperse droplets ranging from a few micrometers to a few nanometers in size can be produced, resulting in a uniform coating. The size of the droplets can be controlled readily by altering the voltage applied at the capillary nozzle and the flow rate of the liquid. In addition, ESD can be performed under ambient conditions. Typically, the deposition efficiency is high and the material consumption rate is low, because the droplets accelerated towards the grounded substrate where nearly all of them are collected.

In this study, we employed ESD onto a nickel foil to create a thin film composite consisting of binder-free ZnO NPs decorated on graphene. When these composite electrodes were used in SCs, the ZnO NPs anchored on the graphene sheets increased the number of electrochemically active sites while also forming a 3D conducting network for electron transfer during the charge/discharge process. The cyclic voltammograms (CVs) and galvanostatic charge/discharge curves of the composite were measured using a three-electrode cell and a symmetric cell, respectively, in the presence of a neutral aqueous electrolyte (1 M Na₂SO₄).

2. Materials and methods

2.1. Synthesis of ZnO/graphene composite by ESD

The precursor solutions for the ZnO/graphene composite were prepared using zinc acetate dihydrate (ZnAc, Zn (CH₃COO)₂·2H₂O,

Oriental Chemical Industries) and graphene (N002-PDR, Angstrom Materials) as the source materials. The concentration of ZnAc was fixed at 75 mM while that of graphene was varied to produce weight ratios of 0.06, 0.13, and 0.18 wt% with respect to the total solution mass, as listed in Table 1. The samples formed using the different graphene concentrations are labeled as ZG-1, ZG-2, and ZG-3, respectively. During a typical synthesis process, a suitable amount of graphene was dispersed in ethanol to form a homogeneous dispersion. Further, ZnAc (75 mM) was dissolved in propylene glycol (PG, C₃H₈O₂, Reagents Duksan) by stirring at room temperature. Next, the graphene dispersion was added to the ZnAc-PG solution and the mixture was subjected to ultrasonication for 90 min, so that the ZnAc solution was coated uniformly over the exfoliated graphene sheets. Then, a potassium hydroxide (KOH, 0.25 M, Sigma-Aldrich) solution was added to this mixture in a dropwise manner. The dispersion was then subjected to ultrasonication for another 20 min. This resulted in the growth of ZnO NPs on the graphene sheets. In addition, a ZnO NP dispersion free of graphene was also formed using a PG/ethanol solution. This graphene-free ZnO NP dispersion as well as the different ZnO NP/graphene dispersions were used for ESD on nickel foil.

Fig. 1a and b shows the procedure for preparing the precursor solutions as well as a schematic of the ESD setup, which consisted of a syringe, a nozzle, a grounded collector, and a high-voltage supply. The pristine ZnO NP dispersion and the ZnO NP/graphene dispersions were electro sprayed on pieces of pre-cleaned nickel foil heated to 90 °C. The voltage applied to the nozzle was 11 kV, and the distance between the substrate and the nozzle was 6 cm. The fabricated samples were heated to 300 °C in argon at a heating rate of 3°/min then annealed at that temperature for 30 min. Fig. 1 (c) shows the surface morphologies of the electro sprayed films formed using the pure ZnO NP dispersion and using the ZnO NP/graphene dispersions.

The synthesized electrodes were characterized using a range of techniques to evaluate the properties of the composite material. X-ray diffraction (XRD) analysis (D/max-2500, Rigaku, Japan) was used to study the crystal structures of the samples. A Raman spectrometer (NRS-3100, Jasco) was used to analyze the structural changes in the samples. The samples were imaged using field-emission scanning electron microscopy (FE-SEM, S-5000, Hitachi, Ltd.) and transmission electron microscopy (TEM, JEM 2100 F, JEOL Inc.). X-ray photoelectron spectroscopy (XPS, Theta Probe Base System, Thermo Fisher Scientific Co.) was performed to determine the chemical states of the constituent elements of the composite samples.

2.2. Electrochemical measurements

Electrochemical measurements including cyclic voltammetry and electrochemical impedance spectroscopy (EIS) were performed with a potentiostat (VersaSTAT-3, Princeton Applied Research, USA). The ZnO/graphene composite electrodes were tested using a three-electrode cell consisting of a Ag/AgCl reference electrode, platinum counter electrode, and the ZnO/graphene composite as the working electrode. AC impedance measurements were performed for frequencies of 0.1–10⁵ Hz. Symmetric coin cells

Table 1
Precursor composition.

| Case | Graphene (wt%) |
|--------------|----------------|
| ZG -1 | 0.06 |
| ZG -2 | 0.13 |
| ZG -3 | 0.18 |

Bold indicates the best case of this work.

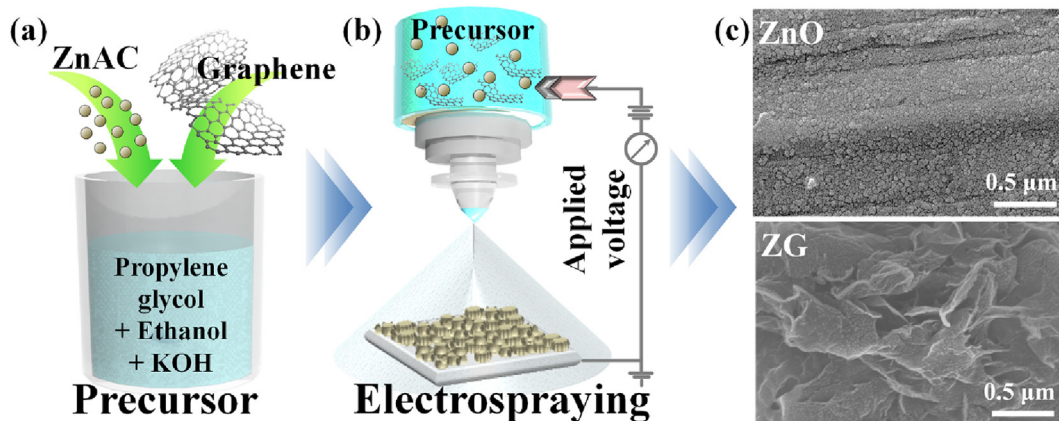


Fig. 1. ZnO/graphene composite: (a) precursor solution preparation, (b) schematic of electrospaying setup used for deposition, and (c) morphologies of a pure ZnO NP film and a ZnO NP/graphene composite film (ZG).

(CR2032) were used for the galvanostatic charge/discharge measurements, which were performed with a WBCS3000 battery testing system (WonATech, Seoul, South Korea). The coin cells were prepared using two ZnO/graphene electrodes (14 mm in diameter), which were electrically isolated using a polymer separator (Celgard 3501, Celgard, Chungbuk, South Korea). All the electrochemical measurements were carried out in a 1 M Na₂SO₄ solution as the electrolyte.

3. Results and discussion

3.1. Structural analysis

Fig. 2 shows the XRD patterns of graphene, the pristine ZnO NPs, and the ZnO/graphene composite (ZG-2). The pristine graphene (bulk) shows a broad peak between 20 and 30° with hump at 24.5°. This peak slightly shifted to higher diffraction angle in the composite film, as marked by '♦'. Peaks observed at 2θ values of 31.78, 34.40, 36.26, 47.58, 56.65, 62.89, 67.7, 68.9 and 76.9° correspond to the (100), (002), (101), (102), (110), (103), (112), (201) and (202) planes, respectively, in the hexagonal wurtzite structure of ZnO (JCPDS Card No. 80–0075). A few minor peaks attributable to Zn(OH)₂ (JCPDS Card No. 38–0356) are also observed, as marked with solid circle (●). The presence of this impurity phase may be due to low post treatment temperature. Further, the crystallite size of the NPs was estimated using the Debye-Scherrer equation (Eq. (1)) and the XRD data:

$$D = 0.9\lambda/\beta \cdot \cos \theta \quad (1)$$

where D is the crystallite size, λ is the wavelength of the X-rays, β is the full width at half maximum, and θ is the diffraction angle.

The average crystallite sizes for the pristine ZnO NPs and those in the composite were found to be approximately 18 and 14 nm, respectively. The XRD pattern of ZG-2 shows lower-intensity and slightly broadened ZnO peaks compared to the pure ZnO sample, reflecting the decrease in crystallite size of ZnO NPs in the presence of graphene. Furthermore, to test for preferential orientation of the ZnO NPs, the textural coefficient (TC) of ZnO NP and ZG-2 was calculated (see Table S1), as shown in supporting information, for diffraction planes of (100), (002) and (101). The resulting TC indicated that the film of ZnO NPs have (002) as a preferred orientation. However, for ZG-2, (100) orientation was slightly preferred. This is consistent with qualitative observations of the relative intensities of the three peaks in Fig. 2. This change in preferred orientation

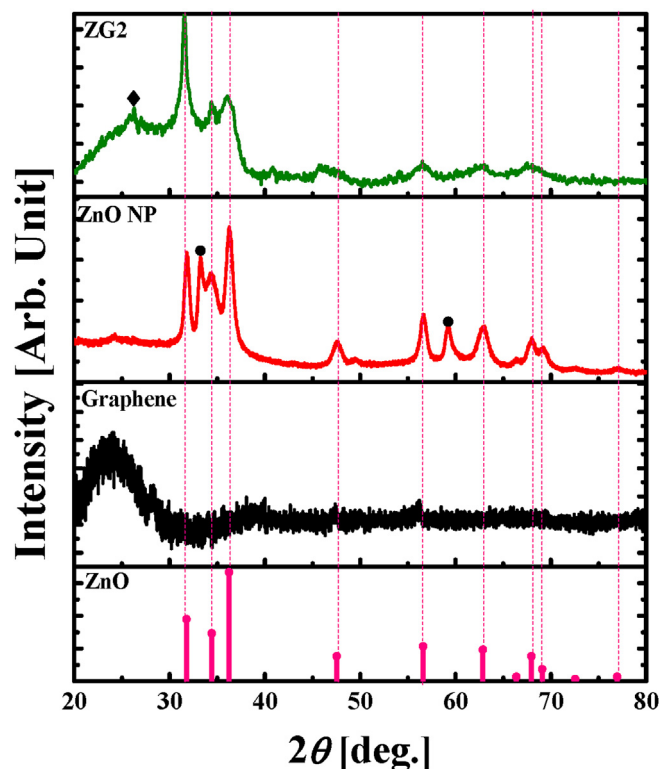


Fig. 2. X-ray diffraction patterns of graphene, ZnO NPs, and ZnO/graphene composite sample ZG-2.

illustrates the strong interaction between the graphene sheets and ZnO NPs, which is expected to improve their performance in SCs.

The Raman spectra of graphene, the ZnO NPs, and the ZnO/graphene composite samples containing graphene at different concentrations are shown in Fig. 3. Wurtzite ZnO exhibits Raman active phonon modes E_2 (low and high frequencies), A_1 (transverse optic (TO) and longitudinal optic (LO)), and E_1 (TO and LO). These modes were observed in the ZnO NP film and all the composites, as shown in Fig. 3a. Nonpolar phonon modes with symmetry, such as the E_2 mode, have two frequencies; E_2 -high is associated with the vibrations of O₂ atoms, while E_2 -low is associated with the vibrations of the Zn sublattice [33]. The peaks observed at 430, 538, and 1078 cm⁻¹ correspond to the non-polar optical phonon E_2 (high), E_1

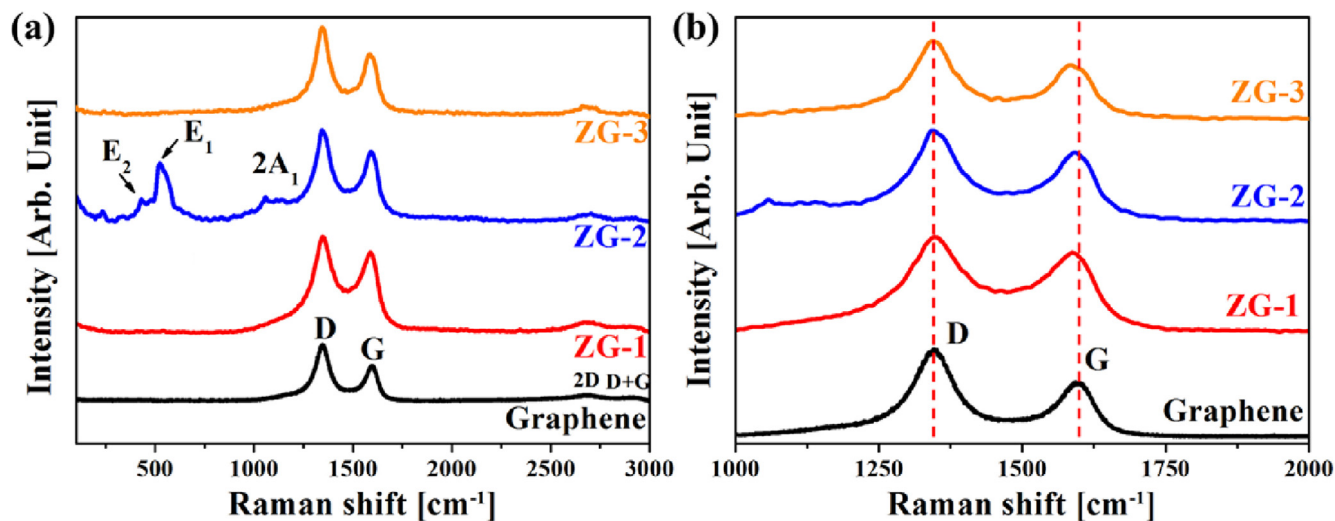


Fig. 3. Raman spectra of various ZnO/graphene composites showing (a) phonon modes of ZnO and (b) D and G bands of graphene.

(LO), and A_1 (LO) modes of wurtzite ZnO. The longitudinal optical phonon modes E_1 (LO) and A_1 symmetry (A_1 (LO)) are related to the non-stoichiometric defects present in ZnO.

Raman scattering is also used widely for analyzing graphene and its defects. The presence of defects in the graphene part of the composite samples was confirmed by an analysis of the D and G bands, as shown in Fig. 3b. Pure graphene exhibits two sharp peaks, at $\sim 1343 \text{ cm}^{-1}$ and $\sim 1597 \text{ cm}^{-1}$, respectively; these correspond to

the D and G bands, respectively, of graphene. The D band at approximately 1343 cm^{-1} corresponds to disordered carbon, while the G band at 1596 cm^{-1} is related to the phonon vibrations of sp^2 -hybridized carbon. The I_D/I_G ratio is a measure of the concentration of defects in graphene [34]. The changes in the positions of the D and G bands and the I_D/I_G ratio are presented in Table 2. The increase in the I_D/I_G ratio from 1.17 for ZG-1 to 1.39 for ZG-3 indicates that the number of defects increased with an increase in the graphene concentration. The trend toward increasing defect concentration with higher graphene content is consistent with observations for pure graphene with I_D/I_G ratio of 1.61.

Table 2
Raman peaks and their intensity ratio for various composites.

| Case | D peak [cm^{-1}] | G peak [cm^{-1}] | I_D/I_G |
|--------------|-----------------------------|-----------------------------|-------------|
| ZG -1 | 1346 | 1588 | 1.17 |
| ZG -2 | 1342 | 1590 | 1.30 |
| ZG -3 | 1343 | 1584 | 1.39 |
| Graphene | 1347 | 1597 | 1.61 |

Bold indicates the best case of this work.

3.2. Morphological analysis

The morphologies of the pristine ZnO NPs and the ZnO/graphene composites were evaluated using SEM as presented in Fig. 4. The SEM images were also processed using MATLAB to enhance

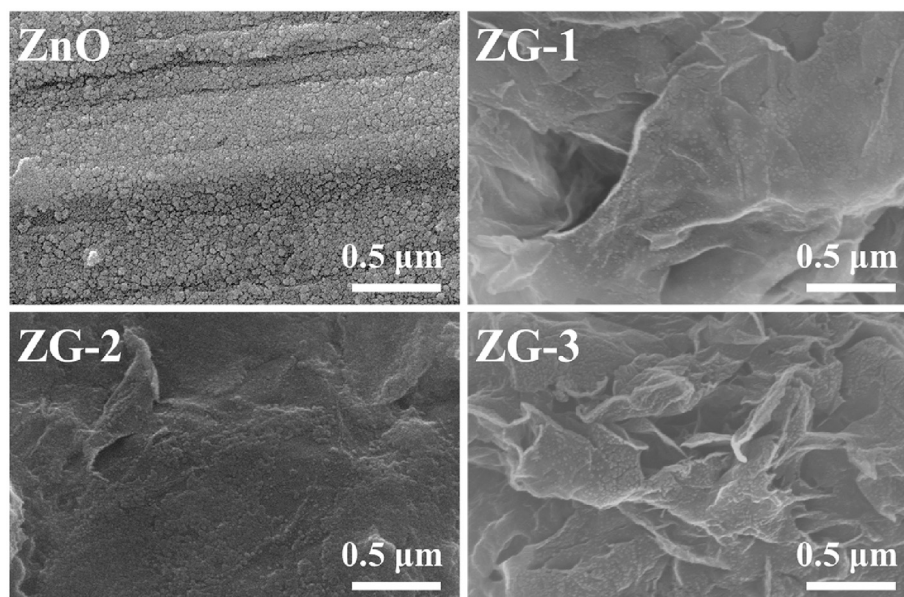


Fig. 4. SEM images of ZnO NPs and ZnO/graphene composites.

their contrast by converting the grayscale range into a colormap (see supporting information Fig. S1). Figure 4a shows that large ZnO NPs were deposited over the nickel foil and that they aggregated and coalesced. The large size of the coalesced NPs is even more evident in the lower resolution image in Fig. S2. The agglomeration phenomenon may be attributable to the strong intermolecular forces between the NPs in the absence of carbon or a surfactant, which allowed them to increase in size and combine with the other growing particles through physical or chemical adsorption. However, the agglomeration of the ZnO NPs was restricted to a certain degree in ZnO/G composites because of the following three factors: a) the uniform coating of the ZnAc solution over graphene resulted in a controlled reaction with KOH, leading to heterogeneous nucleation of a high density of NPs on the graphene support; b) the growth of the ZnO particles was primarily along the (100) plane, as confirmed by XRD analysis (Fig. 2), because graphene and ZnO have similar hexagonal structures; and c) owing to the exfoliation of graphene and its use in the appropriate concentration, the ZnO NPs were well distributed on the surfaces of the graphene sheets, as confirmed by the SEM images of ZG-1, ZG-2, and ZG-3 in Fig. 4. The growth of the ZnO NPs on graphene can be explained as follows. The Zn^{2+} ions are adsorbed onto graphene via electrostatic

interactions. The graphene sheets act as nucleation centers for the Zn ions, leading to the formation of a seed layer a few nanometers in size; these seeds grow further into spherical ZnO NPs. In the SEM image of ZG-1 (Fig. 4), one can see that the graphene sheets are exfoliated. This restricted the number of NPs that could grow, as the concentration of graphene was low. However, the presence of a lower amount of graphene in ZG-1 meant that the relative concentration of ZnAc was higher than those in the cases of ZG-2 and ZG-3. Therefore, the size of the ZnO NPs was larger in many locations (i.e., at the bright spots and regions, which are mostly observed at the edges of the graphene sheets). In contrast, in the case of ZG-3 (see Fig. 4), although the degree of agglomeration was lower (fewer bright spots), the graphene sheets were more crumpled than the exfoliated ones. Thus, the total number of electrochemically active sites for ion adsorption was lower as compared to the number of sites for the redox reactions responsible for the pseudocapacitance. In the case of ZG-2, an appropriate number of ZnO NPs were decorated on the graphene sheets, resulting in the formation of a suitable path for ion transport and hence an improvement in electrochemical activity.

Fig. 5a shows a TEM image of the ZnO/graphene composite ZG-2. It shows that the ZnO NPs are uniformly decorated on the

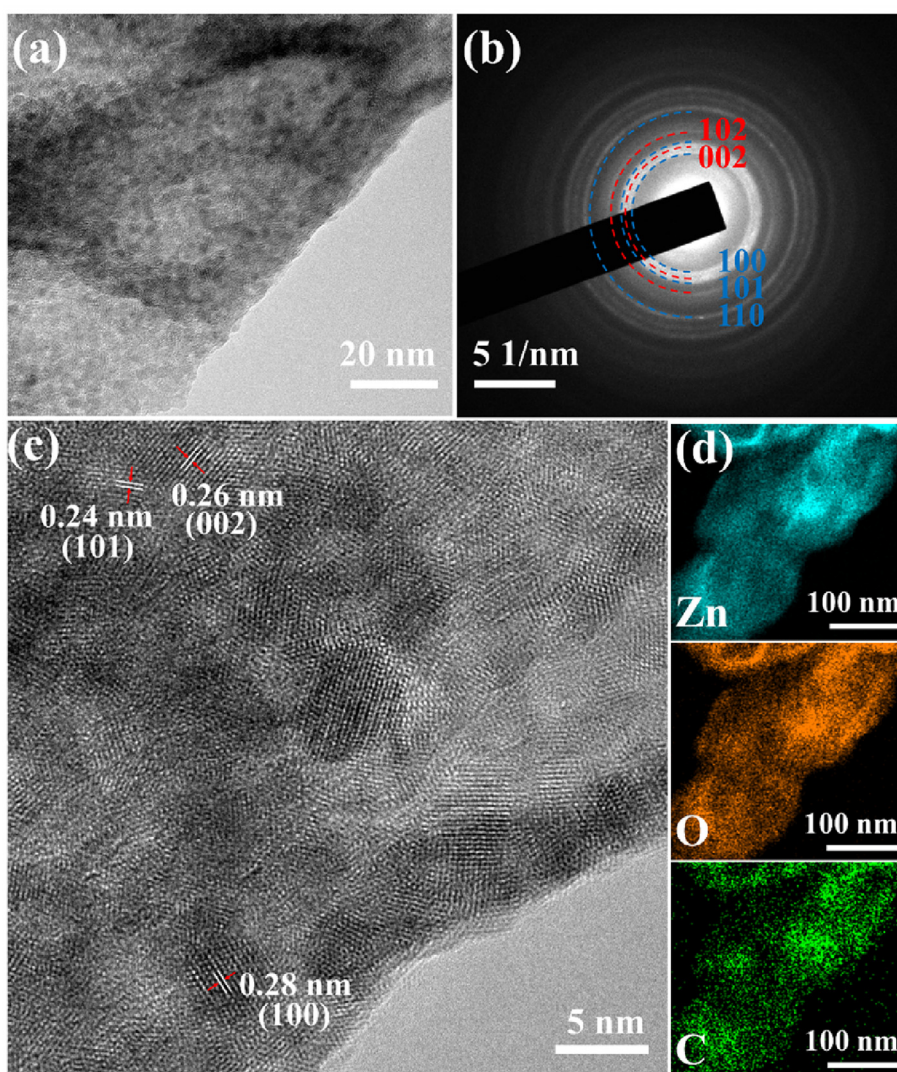


Fig. 5. (a) TEM image, (b) SAED pattern, (c) HRTEM image, and (d) elemental maps of Zn, O, and C for ZnO/graphene composite (ZG-2).

graphene sheets, as also indicated by the SEM images. Fig. 5b shows the selected area electron diffraction (SAED) pattern of the composite. The diffraction ring pattern confirms the crystallinity of the NPs, and the rings can be indexed to the (100), (002), (101), (102), and (110) planes of wurtzite ZnO. Fig. 5c shows a high-resolution TEM (HRTEM) image of the surface region of the ZnO-loaded graphene composite. The lattice fringes in the HRTEM image correspond to the (100) plane of hexagonal ZnO and have a spacing of 0.28 nm. It also shows regions where the (002) and (101) planes of ZnO are visible, with spacing of 0.26 and 0.24 nm, as expected from the SAED and XRD analysis. Elemental maps for Zn, C, and O shown in Fig. 5d further confirm that the ZnO NPs were distributed homogeneously on the graphene sheets.

3.3. XPS analysis

The chemical states of the constituent elements present in the ZnO/graphene composite were examined by XPS. Fig. 6a shows the XPS survey spectrum of the ZnO/graphene composite (ZG-2). The spectrum exhibits peaks characteristic of Zn, O, and C. The high resolution core level XPS spectra for Zn, O, and C are shown in Fig. 6b–d. The two peaks observed at binding energies of 1022 and 1045 eV in the core level Zn2p spectrum correspond to the $2p_{3/2}$ and $2p_{1/2}$ orbitals, respectively. The spin-orbit splitting of 23 eV between the peaks corresponds to the Zn^{2+} state. Moreover, the absence of a peak at 1021.5 eV confirmed that Zn was present only in the oxidized state. No peaks related to metallic Zn were observed [35]. The O1s peak of the ZnO/graphene composite could be deconvoluted into three peaks, which appear at 530.0, 531.2, and 532.2 eV. The peak at the lower binding energy (530 eV) corresponds to O atoms in the wurtzite structure of hexagonal ZnO. The second peak, which appears at 531.2 eV, can be assigned to the O^{x-} ions (O^- and O^{2-} ions) in oxygen-deficient regions within the ZnO

matrix. Finally, the third peak, which appears at a binding energy at 532.2 eV, represents adsorbed oxygen or OH^- . These results support the conclusion that ZnO NPs were formed in a uniform manner on the surfaces of the graphene sheets. The core level C1s spectrum of the ZnO/graphene composite is shown in Fig. 6d. The deconvoluted spectrum of the composite exhibits three distinct peaks, which are located at 284.5 (C–C bonds), 285.5 (C–O bonds), and 289.4 eV (O–C=O bonds). The intensity of the peaks corresponding to the oxygen functional groups is lower than that for the peak related to the C–C bond, implying that the concentration of defects in graphene due to oxidation is negligible [36].

3.4. Electrochemical measurements

Fig. 7 shows the CV curves of the ZnO/graphene composite electrodes over a potential range from -0.6 to 0.3 V. Their electrochemical performance was characterized at scan rates of 10 – 300 $mV s^{-1}$. As stated above, the number of ZnO NPs formed increased with increasing graphene concentration. The variations in the intensities of the D and G bands in the Raman spectra (Fig. 3) as well as the surface morphologies of the composite samples as observed by SEM (Fig. 4) confirmed the formation of a larger number of ZnO NPs for a higher graphene concentration. This phenomenon was attributable to the large surface area of the exfoliated graphene sheets providing more hosting sites for the growth of the ZnO NPs. Therefore, we expected that the ZnO/graphene electrodes would show better electrochemical performance owing to the following factors: a) their improved conductivity and EDL capacitance (attributable to graphene) and b) their higher redox reactivity (attributable to the formation of a large number of ZnO NPs), which would result in an increase in their pseudocapacitance.

The CVs for all the ZnO/graphene composites were quasi-

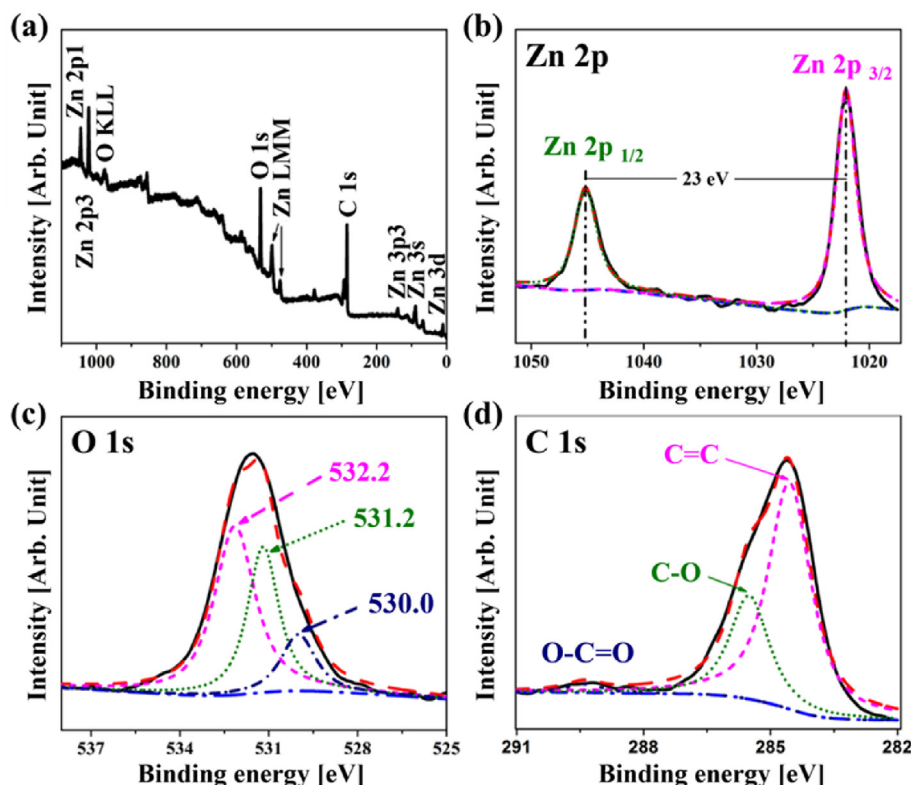


Fig. 6. (a) XPS survey spectrum of ZnO/graphene composite ZG-2. Core level (b) Zn2p, (c) C1s, and (d) O1s spectra of the composite.

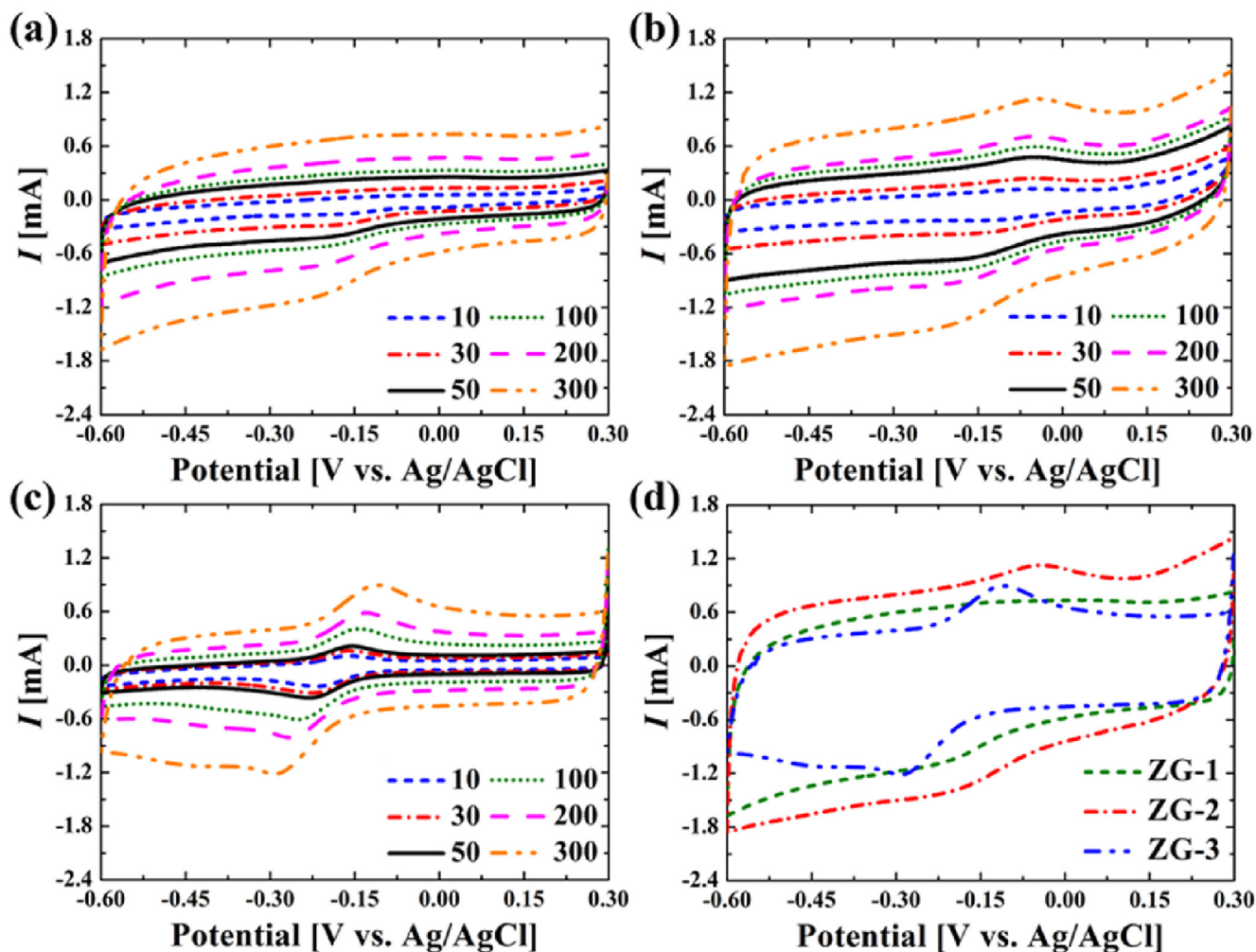


Fig. 7. CV curves of ZnO/graphene composite electrodes at different scan rates: (a) ZG-1, (b) ZG-2, and (c) ZG-3 for scan rates of 10–300 mV s^{-1} and (d) combined plot for all three electrodes at scan rate of 300 mV s^{-1} .

rectangular. However, in the cases of ZG-2 and ZG-3, redox peaks were observed at approximately -0.15 and -0.28 V, respectively, in the cathodic section. On the other hand, the corresponding anodic redox peaks were present at -0.05 and -0.15 V in the cases of ZG-2 and ZG-3, respectively. These redox peaks were related to the direct adhesion of the colloidal NPs on the Ni foil. Furthermore, several reports have suggested that the pseudocapacitive redox peaks of ZnO are suppressed because of their superposition with those related to the EDL capacitance of graphene. Fig. 7a–c shows that the electrodes exhibited capacitive characteristics over the investigated potential range, both at low scan rates (10 mV s^{-1}) and very high scan rates (300 mV s^{-1}). In addition, the CVs of the electrodes obtained at the different scan rate were similar, indicating that the electrodes underwent reversible redox reactions. Further, with an increase in the scan rate, the integrated area under the CV increased owing to an increase in the electrochemical response in terms of the current output [37]. This behavior can be explained as follows: the electrolytic ions diffuse deep within the electrode material, with partial trapping occurring at low scan rates. On the other hand, at higher scan rates, the potential difference between the anodic and cathodic peaks increases owing to the polarization of the electrode [38]. For comparison, the CV curve of pure Ni, graphene and ZnO NP on Ni foil are shown in Fig. S3.

The synergistic effect of the ZnO NPs and graphene is likely the

primary cause for the observed enhancement in the electrochemical properties. However, when the ratio of ZnAc to graphene was varied from the optimal one, which was 0.75:0.13 (i.e., that corresponding to ZG-2), to 0.75:0.06 (ZG-1) or 0.75:0.18 (ZG-3), the corresponding composites showed inferior electrochemical performance. In the case of ZG-1, while the graphene sheets were exfoliated, the number of ZnO NPs formed was low, as shown in Fig. 4. On the other hand, in the case of ZG-3, the number of ZnO NPs formed was high but the graphene sheets were not exfoliated to the desired degree (see Fig. 4) owing to the higher concentration of graphene. As explained above, based on the morphological analysis, at a lower graphene concentration (ZG-1), the formation of fewer ZnO NPs on the graphene sheets led to their restacking in the presence of the electrolyte during the electrochemical tests. Thus, owing to the restacking of the graphene sheets, the ZG-1-based electrode had fewer accessible electrochemically active sites. On the other hand, in the case of the composite with a higher graphene concentration (ZG-3), the graphene sheets were not adequately exfoliated, but were crumpled, and the ZnO NPs agglomerated in several places, as confirmed by the SEM images. Thus, the presence of a greater number of ZnO NPs and crumpled graphene limited ion/electron transport in the corresponding electrode, leading to relatively poorer electrochemical performance. For these reasons, ZG-2 showed superior electrochemical

performance as compared to ZG-1 and ZG-3, as shown in Fig. 7d. The areal capacitance estimated from CV curves, presented in Fig. S4, clearly shows the higher capacitance of ZG-2. Thus, the performance of ZG-2 can be attributed to optimal ZnO NP growth on well-exfoliated graphene sheets, owing to which enough electrochemically active sites were present for ion diffusion as well as for efficient ion and charge transfer during the electrochemical redox reaction. The reversible redox reaction between the ZnO NPs and the electrolyte (1 M Na₂SO₄), which leads to pseudocapacitance, can be described as follows:



Fig. 8 a-c show the galvanostatic charge/discharge curves of the ZG-1, ZG-2, and ZG-3 electrodes at current densities of 1–4 mA·cm⁻² for a potential difference between the electrodes in a symmetric cell of 0–0.9 V. For all the current densities, the curves are triangular and almost symmetrical, with no clear voltage drop being observed for any of the electrodes. This indicates that all the electrodes underwent a capacitive faradaic redox reaction at the electrode/electrolyte interface. The figures also show that the charging and discharging time of ZG-2 is higher than those of ZG-1, and ZG-3, indicating that ZG-2 had a higher capacitance. The capacitances of ZG-1, ZG-2, and ZG-3 as obtained from their charge/discharge

curves at the different current densities are presented in Fig. 8d. The capacitance was calculated using the following equation:

$$C_a = \frac{I \cdot \Delta t}{\Delta V \cdot A} \quad (3)$$

where I , Δt , ΔV , and A are the discharge current (A), discharge time (s), discharge voltage (V), and total area (cm²), respectively. To highlight the superior electrochemical performance of the composite electrodes fabricated in this study, their areal capacitances were compared with those of similar electrodes reported previously (see Table 3). This comparison clearly shows that the areal capacitances of the electrodes fabricated in this study are higher than those of the other ZnO-based SC electrodes.

Further, we investigated the long-term cycling performance of the ZG-2 electrode through galvanostatic charge/discharge measurements performed at a current density 1.5 mA·cm⁻² for 1000 cycles, as shown in Fig. 9a. The inset of Fig. 9a shows the charge/discharge curves corresponding to the first and last three cycles. The galvanostatic curves remain almost unchanged even after 1000 cycles, confirming the stability of the electrode. The retention rate of the electrode was approximately 90% after 1000 cycles of charging/discharging at 1.5 mA·cm⁻². Fig. 9b shows the performance of the ZG-2 electrode in the form of a Ragone plot (energy

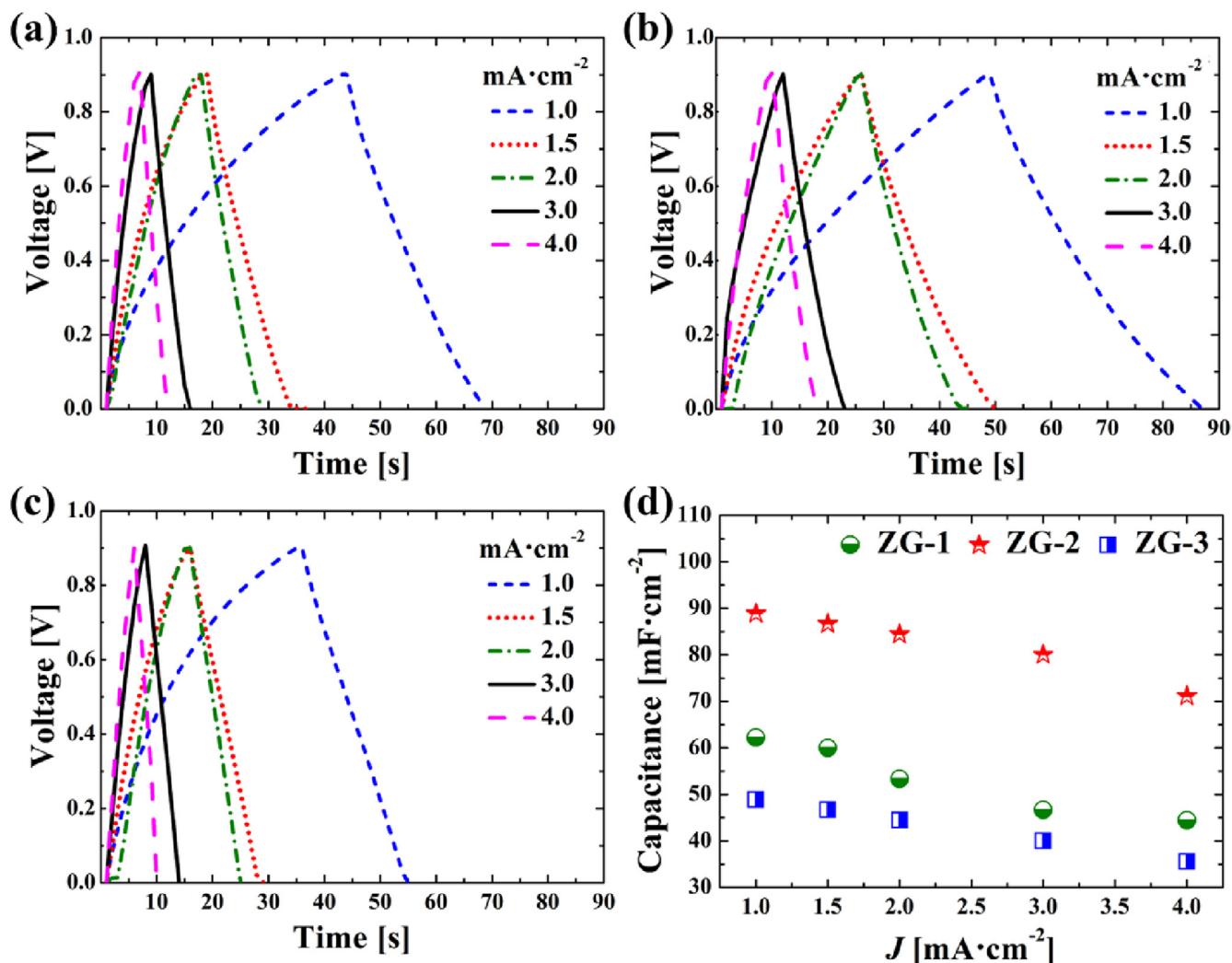


Fig. 8. Galvanostatic charge/discharge curves of (a) ZG-1, (b) ZG-2, and (c) ZG-3 and (d) their areal specific capacitances at different current densities.

Table 3

Comparison of specific capacitance of composite electrode fabricated in this study and those of other electrode materials reported previously (^aPVA/LiCl gel, ^bNa₂SO₄, ^cPMMA-PC-LiClO₄ gel, and ^dNaNO₃) (R3-6).

| Materials | Capacitance [mF·cm ⁻²] | Current density [mA·cm ⁻²] | Potential window [V] | Electrolyte | Ref. |
|--|------------------------------------|--|----------------------|------------------------|----------------|
| ZnO@amorphous ZnO-doped MnO ₂ | 138 | 1 | 0–0.8 | ^a | [3] |
| ZnO Nanorod | 31.3 | 0.02 | –0.2–0.6 | – | [6] |
| ZnO Nanowire | 49 | 1 | 0–0.5 | 0.5 M ^b | [8] |
| Graphene/ZnO | 2.6 | 0.2 | 0–1.6 | ^c | [9] |
| ZnO/MnO | 1.8 | 2 mV s ⁻¹ | –0.4–1.2 | 0.1 M ^b | [15] |
| ZnO/PPy | 2 | 10 mV s ⁻¹ | –0.25–0.75 | 0.5 M ^d | [16] |
| ZnO Nanorods | 29.4 | 5 mV s ⁻¹ | –1–0 | 1 M ^b | [17] |
| ZnO NPs/Graphene | 89 | 1 | 0–0.9 | 1 M^b | Present |

Bold indicates the best case of this work.

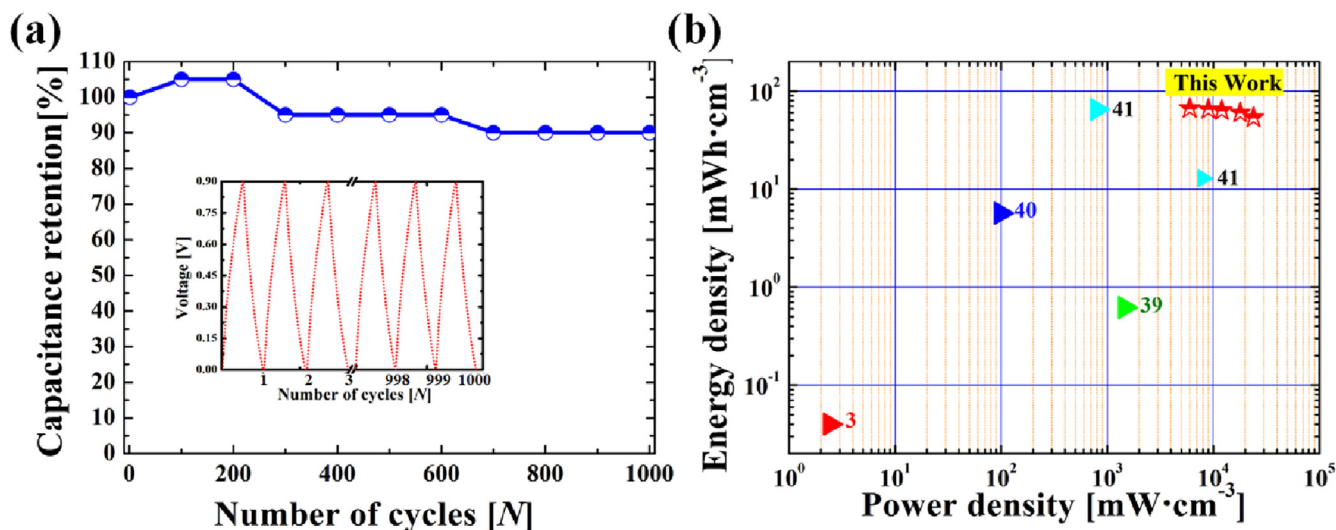


Fig. 9. (a) Capacitance retention vs. number of cycles and (b) Ragone plot of ZG-2 in comparison to previously-reported ZnO-based electrodes.

density vs. power density); the values for similar electrodes reported previously are also shown for comparison [3,39–41]. The ZG-2 electrode exhibited energy and power densities of 67 mWh·cm⁻³ and 6000 mW·cm⁻², respectively, at a low current density (1 mA·cm⁻²). At 4 mA·cm⁻², ZG-2 showed energy and power densities of 53 mWh·cm⁻³ and 24000 mW·cm⁻², respectively. The energy and power densities were calculated using the following equations [41].

$$E = \frac{1}{2} \cdot C_s \cdot \Delta V^2 \left[\text{mW} \cdot \text{h} \cdot \text{cm}^{-3} \right] \quad (4)$$

$$P = \frac{E}{\Delta t} \left[\text{mW} \cdot \text{cm}^{-3} \right] \quad (5)$$

where E is the energy density, C_s is the specific capacitance, ΔV is the potential window, Δt is the discharge time, and P is the power density.

The high energy density of the electrode at a low current density can be attributed to the enhanced pseudocapacitance of the electrode because of efficient electrolyte ion diffusion in the active material during the faradaic redox reaction. In addition, at a higher current density, the composite electrode showed better power-handling performance (see Fig. 9b).

To study charge transport and ionic diffusion at the electrode/electrolyte interface in greater depth, EIS was performed on all three ZnO/graphene composite electrodes. Fig. 10 shows the Nyquist plots for the different ZnO/graphene composite samples. The plots for ZG-2 and ZG-3 exhibit a semicircle in the high-

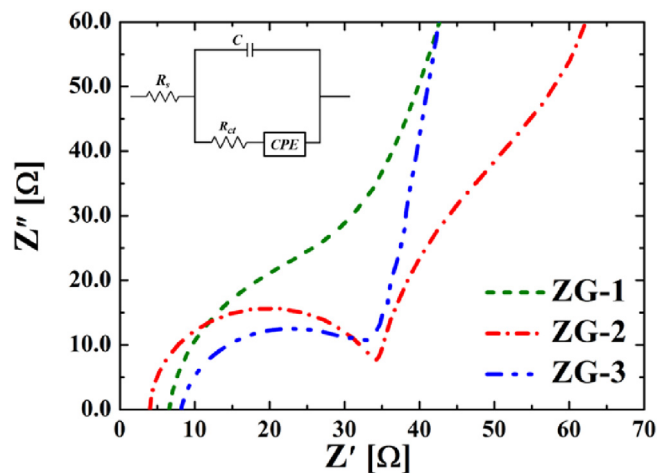


Fig. 10. Nyquist plots of ZnO/graphene composite samples: (a) ZG-1, (b) ZG-2, and (c) ZG-3.

frequency region and a straight line in the low-frequency region. On the other hand, ZG-1 does not exhibit a complete semicircular arc, probably owing to its lower graphene concentration; this probably resulted in fewer electrochemically active sites being present. However, for all three cases, a straight line can be seen in the mid-to-low frequency region, confirming that the diffusion of ions from the electrolyte to the electrode occurred readily. This

Table 4
Parameters calculated from Nyquist plot.

| Sample | ZG-1 | ZG-2 | ZG-3 |
|-----------------------|----------------------|----------------------|----------------------|
| R_s (Ω) | 6.8 | 4.3 | 8.6 |
| C (F) | 9.5×10^{-5} | 3.4×10^{-5} | 2×10^{-5} |
| R_{ct} (Ω) | 48 | 48.5 | 29 |
| CPE | 6.5×10^{-4} | 1.2×10^{-4} | 6.8×10^{-4} |

straight line in the mid-to-low frequency regime in the real impedance versus imaginary impedance curve represents the Warburg impedance. Further, the semicircle observed in the low real-impedance region indicated that the solution resistance (R_s) was low and that efficient charge transfer occurred during the electrochemical reaction. The intercept of the semicircle on the x -axis indicates the bulk solution impedance or the solution resistance. Further, the charge transfer resistance (R_{ct}) arising at the electrode/electrolyte interface can be calculated by measuring the diameter of the semicircle at the x -axis. That the diameter was small in all the cases indicated that the ZnO NPs were well bonded to the graphene sheets, allowing efficient charge transfer between ZnO and graphene.

The parameters calculated by fitting the above-described Nyquist plots (Fig. 10) are listed in Table 4. The lower series resistance between the electrode and the electrolyte in the case of ZG-2 contributed significantly to its improved capacitance. The CPE is the constant phase element and is related to the capacitance at the electrode/electrolyte interface. The value of R_{ct} for ZG-3 was lower than that for the other composites, owing to the higher graphene concentration of the former. However, the morphological structures of the various composite samples, shown in Fig. 4d, suggest that the ZnO NPs in ZG-3 underwent agglomeration, which inhibited the diffusion of electrolyte ions, and that the graphene surface area was reduced, owing to the inadequate exfoliation of the graphene sheets. The latter phenomenon may be attributable to the use of low amounts of PG and ethanol. The above-stated factors explain why ZG-3 exhibited relatively poorer electrochemical performance, as can be observed from Figs. 7d and 8d.

4. Conclusions

A non-vacuum-based ESD technique was employed for the first time in the synthesis of a binder-free ZnO/graphene composite for use as an electrode material in SCs. In contrast to other methods for producing such composites, the proposed method does not involve multiple steps for electrode preparation. The optimized ZnO/graphene composite electrode, ZG-2, exhibited a typical pseudorectangular CV. This was indicative of its good capacitive performance, with the electrode showing a specific capacitance of $89 \text{ mF} \cdot \text{cm}^{-2}$ at a current density of $1 \text{ mA} \cdot \text{cm}^{-2}$. Moreover, a symmetric cell based on this composite electrode showed volumetric energy and power densities of $67 \text{ mWh} \cdot \text{cm}^{-3}$ and $6000 \text{ mW} \cdot \text{cm}^{-3}$, respectively, at $1 \text{ mA} \cdot \text{cm}^{-2}$. Further, after being charged/discharged for 1000 cycles, the symmetric cell retained 90% of its original capacitance. This confirmed that the electrode was highly electrochemically stable. The superior electrochemical performance of the electrode can be attributed to the uniform distribution of the ZnO NPs on the graphene sheets, which hindered the agglomeration of the NPs and prevented the restacking of the graphene sheets.

Acknowledgement

This research was supported by the Technology Development Program to Solve Climate Changes of the National Research Foundation (NRF) funded by the Ministry of Science, ICT & Future

Planning (NRF-2016M1A2A2936760). This research was also supported by NRF-2013M3A6B1078879, NRF-2017R1A2B4005639, and NRF-2016R1A2B3009481.

Appendix A. Supplementary data

Supplementary data related to this article can be found at <https://doi.org/10.1016/j.jallcom.2017.12.320>.

References

- [1] Y. Huang, H. Li, Z. Wang, M. Zhu, Z. Pei, Q. Xue, Y. Huang, C. Zhi, Nanostructured polypyrrole as a flexible electrode material of supercapacitor, *Nano Energy* 22 (2016) 422–438.
- [2] P. Lu, D. Xue, H. Yang, Y. Liu, Supercapacitor and nanoscale research towards electrochemical energy storage, *Int. J. Smart Nano Mater.* 4 (2013) 2–26.
- [3] X. Xiao, P. Yang, Y. Li, Y. Ding, P. Qiang, X. Tan, W. Mai, Z. Lin, W. Wu, T. Li, H. Jin, P. Liu, J. Zhou, C.P. Wong, Z.L. Wang, Hydrogenated ZnO core shell nanocables for flexible supercapacitors and self-powered systems, *ACS Nano* 7 (2013) 2617–2626.
- [4] M. Sreejesh, S. Dhanush, F. Rossignol, H.S. Nagaraja, Microwave assisted synthesis of rGO/ZnO composites for non-enzymatic glucose sensing and supercapacitor applications, *Ceram. Int.* 43 (2017) 4895–4903.
- [5] A. González, E. Goikolea, J.A. Barrena, R. Mysyk, Review on supercapacitors: technologies and materials, *Renew. Sustain. Energy Rev.* 58 (2016) 1189–1206.
- [6] X. Sun, Q. Li, Y. Lu, Y. Mao, Three-dimensional ZnO@MnO₂ core@shell nanostructures for electrochemical energy storage, *Chem. Commun.* 49 (2013) 4456–4458.
- [7] H. Gao, J. Xiang, Y. Cao, Hierarchically porous CoFe₂O₄ nanosheets supported on Ni foam with excellent electrochemical properties for asymmetric supercapacitors, *Appl. Surf. Sci.* 413 (2017) 351–359.
- [8] X. Zheng, Y. Sun, X. Yan, X. Sun, G. Zhang, Q. Zhang, Y. Jiang, W. Gao, Y. Zhang, High carrier concentration ZnO nanowire arrays for binder-free conductive support of supercapacitors electrodes by Al doping, *J. Colloid Interface Sci.* 484 (2016) 155–161.
- [9] J. Yun, Y. Lim, H. Lee, G. Lee, H. Park, S.Y. Hong, S.W. Jin, Y.H. Lee, S.-S. Lee, J.S. Ha, A patterned graphene/ZnO UV sensor driven by integrated asymmetric micro-supercapacitors on a liquid metal patterned foldable paper, *Adv. Funct. Mater.* (2017), 1700135.
- [10] Y. Yang, S. Ren, X. Song, Y. Guo, D. Si, H. Jing, S. Ma, C. Hao, M. Ji, Sn@SnO₂ attached on carbon spheres as additive-free electrode for high-performance pseudocapacitor, *Electrochim. Acta* 209 (2016) 350–359.
- [11] Y. Dai, S. Tang, S. Vongehr, X. Meng, Silver nanoparticle-induced growth of nanowire-covered porous MnO₂ spheres with superior supercapacitance, *ACS Sustain. Chem. Eng.* 2 (2014) 692–698.
- [12] S. Sun, G. Jiang, Y. Liu, Y. Zhang, J. Zhou, B. Xu, Growth of MnO₂ nanoparticles on hybrid carbon nanofibers for flexible symmetrical supercapacitors, *Mater. Lett.* 197 (2017) 35–37.
- [13] C.-C. Hu, K.-H. Chang, M.-C. Lin, Y.-T. Wu, Design and tailoring of the nanotubular arrayed architecture of hydrous RuO₂ for next generation supercapacitors, *Nano Lett.* 6 (2006) 2690–2695.
- [14] D. Xiang, X. Liu, X. Dong, A facile synthetic method and electrochemical performances of nickel oxide/carbon fibers composites, *J. Mater. Sci.* 52 (2017) 7709–7718.
- [15] X. Zhou, L. Ma, MnO₂/ZnO porous film: electrochemical synthesis and enhanced supercapacitor performances, *Thin Solid Films* 597 (2015) 44–49.
- [16] A. Pruna, Q. Shao, M. Kamruzzaman, J.A. Zapien, A. Ruotolo, Enhanced electrochemical performance of ZnO nanorod core/polypyrrole shell arrays by graphene oxide, *Electrochim. Acta* 187 (2016) 517–524.
- [17] P.R. Deshmukh, Y. Sohn, W.G. Shin, Chemical synthesis of ZnO nanorods: investigations of electrochemical performance and photo-electrochemical water splitting applications, *J. Alloy. Comp.* 711 (2017) 573–580.
- [18] M. Meyyappan, Nanostructured materials for supercapacitors, *J. Vac. Sci. Technol. A* 31 (2013), 050803.
- [19] D. Kalpana, K.S. Omkumar, S.S. Kumar, N.G. Renganathan, A novel high power symmetric ZnO/carbon aerogel composite electrode for electrochemical supercapacitor, *Electrochim. Acta* 52 (2006) 1309–1315.
- [20] L.S. Aravinda, K.K. Nagaraja, H.S. Nagaraja, K.U. Bhat, B.R. Bhat, ZnO/carbon nanotube nanocomposite for high energy density supercapacitors, *Electrochim. Acta* 95 (2013) 119–124.
- [21] J.T.R. Hailiang Wang, Georgi Diankov, Hongjie Dai, Nanocrystal growth on graphene with various degrees of oxidation, *J. Am. Chem. Soc.* 132 (2010) 3270–3271.
- [22] Y.-Z. Liu, Y.-F. Li, Y.-G. Yang, Y.-F. Wen, M.-Z. Wang, A one-pot method for producing ZnO-graphene nanocomposites from graphene oxide for supercapacitors, *Scr. Mater.* 68 (2013) 301–304.
- [23] J.M. Sieben, E. Morallón, D. Cazorla-Amorós, Flexible ruthenium oxide-activated carbon cloth composites prepared by simple electrodeposition methods, *Energy* 58 (2013) 519–526.
- [24] Z.J. Li, B.C. Yang, S.R. Zhang, C.M. Zhao, Graphene oxide with improved

- electrical conductivity for supercapacitor electrodes, *Appl. Surf. Sci.* 258 (2012) 3726–3731.
- [25] V. Stavila, A.A. Talin, M.D. Allendorf, MOF-based electronic and optoelectronic devices, *Chem. Soc. Rev.* 43 (2014) 5994–6010.
- [26] Y. Zhang, H. Li, L. Pan, T. Lu, Z. Sun, Capacitive behavior of graphene–ZnO composite film for supercapacitors, *J. Electroanal. Chem.* 634 (2009) 68–71.
- [27] T. Lu, L. Pan, H. Li, G. Zhu, T. Lv, X. Liu, Z. Sun, T. Chen, D.H.C. Chua, Microwave-assisted synthesis of graphene–ZnO nanocomposite for electrochemical supercapacitors, *J. Alloy. Comp.* 509 (2011) 5488–5492.
- [28] M. Dahnoun, A. Attaf, H. Saidi, A. Yahia, C. Khelifi, Structural, optical and electrical properties of zinc oxide thin films deposited by sol-gel spin coating technique, *Optik* 134 (2017) 53–59.
- [29] J.T.D. Ty, H. Yanagi, Electrochemical deposition of zinc oxide nanorods for hybrid solar cells, *Jpn. J. Appl. Phys.* 54 (2015), 04DK05.
- [30] Z. Shi, A.V. Walker, Zinc oxide chemical bath deposition on functionalized organic thin films: formation of nanorods, nano rockets and nanoflowers, *Thin Solid Films* 606 (2016) 106–112.
- [31] M.G. Mali, H. Yoon, M.-W. Kim, M.T. Swihart, S.S. Al-Deyab, S.S. Yoon, Electrodeposited heterojunction $\text{WO}_3/\text{BiVO}_4$ films with nanotextured pillar structure for enhanced photoelectrochemical water splitting, *Appl. Phys. Lett.* 106 (2015), 151603.
- [32] A. Jaworek, Micro- and nanoparticle production by electrospraying, *Powder Technol.* 176 (2007) 18–35.
- [33] D.I. Son, B.W. Kwon, D.H. Park, W.S. Seo, Y. Yi, B. Angadi, C.L. Lee, W.K. Choi, Emissive ZnO-graphene quantum dots for white-light-emitting diodes, *Nat. Nanotechnol.* 7 (2012) 465–471.
- [34] B. Panigrahy, S. Srivastava, Minuscule weight percent of graphene oxide and reduced graphene oxide modified Ag_3PO_4 : new insight into improved photocatalytic activity, *New J. Chem.* 40 (2016) 3370–3384.
- [35] T.B. Ghosh, Md Nurul Islam, K.L. Chopra, H.N. Acharya, XPS and X-ray diffraction studies of aluminum-doped zinc oxide transparent conducting films, *Thin Solid Films* 280 (1996) 20–25.
- [36] E. György, A. Pérez del Pino, C. Logofatu, A. Duta, L. Isac, Effect of nitrogen doping on wetting and photoactive properties of laser processed zinc oxide-graphene oxide nanocomposite layers, *J. Appl. Phys.* 116 (2014), 024906.
- [37] J.S. Suroshe, S.S. Garje, Capacitive behaviour of functionalized carbon nanotube/ZnO composites coated on a glassy carbon electrode, *J. Mater. Chem. A* 3 (2015) 15650–15660.
- [38] J.H. Chen, W.Z. Li, D.Z. Wang, S.X. Yang, J.G. Wen, Z.F. Ren, Electrochemical characterization of carbon nanotubes as electrode in electrochemical double-layer capacitors, *Carbon* 40 1193–1197.
- [39] X. Wang, B. Liu, R. Liu, Q. Wang, X. Hou, D. Chen, R. Wang, G. Shen, Fiber-based flexible all-solid-state asymmetric supercapacitors for integrated photo detecting system, *Angew. Chem. Int. Ed.* 53 (2014) 1849–1853.
- [40] S. Sarkar, P. Howli, B. Das, N.S. Das, M. Samanta, G.C. Das, K.K. Chattopadhyay, Novel quaternary chalcogenide/reduced graphene oxide-based asymmetric supercapacitor with high energy density, *ACS Appl. Mater. Interfaces* 9 (2017) 22652–22664.
- [41] J. Zhao, C. Li, Q. Zhang, J. Zhang, X. Wang, Z. Lin, J. Wang, W. Lv, C. Lu, C. Wong, Y. Yao, An all-solid-state, lightweight, and flexible asymmetric supercapacitor based on cabbage-like ZnCo_2O_4 and porous VN nanowires electrode materials, *J. Mater. Chem. A* 5 (2017) 6928–6936.